# Dental measurement procedure based on 3D analysis and data processing

Rafael Berenguer-Vidal[1], Rafael Verdú-Monedero[2], Rafael Melendreras-Ruiz[1]

[1]*Universidad Católica de Murcia, 30107 Murcia, Spain*

[2]*Universidad Politécnica de Cartagena, 30202 Cartagena, Spain*

**Abstract**

This paper introduces a novel methodology for the alignment and comparison of 3D digital models of individual dental pieces, aimed at evaluating proficiency in the manipulation of rotary cutting instruments within the discipline of dentistry. The proposed approach comprises three principal stages: precise alignment of the 3D model utilizing a customized reference base, application of a parametric deformable model to transform the non-periodically sampled point cloud into a continuous and regular mesh, and quantitative analysis between pairs of modeled dental pieces. The methodology has been validated through the analysis of dental specimens fabricated from Duroplastic® and digitized using the Aidite® A-IS Pro desktop 3D dental scanner. The results demonstrated a high degree of precision in both alignment and modeling, with mean discrepancies between scans ranging from 0.0055 mm to 0.0165 mm, and maximum errors not exceeding 0.1416 mm across the entire surface of each tooth. The findings indicate that the proposed methodology possesses sufficient accuracy for facilitating comparisons between dental scans, thereby enabling its prospective application within the AIDDA® (Automated International Dental Dexterity Algorithm) system for the objective assessment of dental preparations. This approach permits precise comparisons between teeth carved by instructors and those prepared by students, thereby facilitating automated evaluations of student performance and progress in restorative dentistry competencies.

*Keywords:* 3D scanning, deformable models, 3D alignment, dental measurements

## 1. Introduction

In the scientific literature, there are multiple studies related to 3D technology applied to the field of dentistry. A number of them focus on the educational use of virtual simulation systems and 3D printed teeth [1, 2, 3]. Others analyze the accuracy of different 3D printing techniques for the reproduction of teeth, as well as the optimal digital flow to develop the reproduction process [4, 5, 6].

As far as digitization is concerned, some works as, e.g., [7] highlight the importance of the management software in the final accuracy achieved by dental scanners, whereas other research focuses on the accuracy of scanners depending on the type of tooth [8]. Because of their importance in relation to subsequent manufacturing processes, some works compare the precision and accuracy of different technologies used for digital registration of specific parts, such as implant-supported prostheses [9]. Regarding the accuracy of these technologies, namely 3D lasers and optical scanners, the importance of the alignment methods used to accurately join the point clouds generated in each scan is emphasized in [10] in order to generate the final 3D model mesh. Other studies address the accuracy of the scanning process by comparing real and 3D printed models [11]. The accuracy of the digital model is evaluated in [12] by analyzing specific areas of the geometry, namely the mapping surface of the pulp horn. Other investigations highlight the importance of alignment between models to improve the accuracy of their algorithms for digital registration, i.e., Thin Shell Demons [13], Best Fit [14, 15], Triple Scan Method [16], or to perform measurements such as erosive wear [17]. An interesting study is that developed in [18], which addresses the development of comparative measurements

*Email addresses:* rberenguer@ucam.edu (Rafael Berenguer-Vidal[1]), rafael.verdu@upct.es (Rafael Verdú-Monedero[2]), rmelendreras@ucam.edu (Rafael Melendreras-Ruiz[1])

between 3D models of teeth using three-dimensional digital techniques. The same issue is analyzed in [19] where 3D models obtained from different sources are compared.

The training tools typically used for dental practice, both at undergraduate and postgraduate level, implement training systems that are not very precise and fail to fully cover the necessary competencies and skills of the students. Therefore, the need to innovate arises, through the development of new ones that ensure and facilitate the comprehensive acquisition of all the essential knowledge, skills and work criteria. In this sense, 3D design and digitization technologies [20], image processing [21, 22] and additive manufacturing [23] are the keys to undertake a revolution in teaching methodologies, shortening the process of adaptation of graduates to the reality of the labor market, improving the quality of care and facilitating specialization.

An international patent called "Model for teaching in dentistry disciplines" (ref. WO 2020/208284 A1) [24] has been developed as a first step, which enables the development of bespoke dental models, through the use of different materials, densities and colors, and which also includes compatible means to fix them to a practice phantom [25]. In addition, an unprecedented methodology for teaching in Dentistry is registered, which is called REDES® (Restorative Dentistry Education System - RPI: 08 / 2019 / 984), aimed at the acquisition of complete anatomical knowledge, skills and dexterity in anatomical design, as well as the handling of manual and rotary cutting instruments. To complete the process, a system is designed for the objective assessment of preparations made on dental models. For this purpose, AIDDA® (Automated International Dental Dexterity Algorithm - International Trademark no. 1743550) [26], an algorithm based on the comparison between three-dimensional dental models, where one is the model to be evaluated and the other is the master model, was developed and registered. For this operation, the essential requirement is the 3D digitization of the dental pieces by means of a scanner. Prior to carrying out the comparison operations, it is critical to accurately align the models, a process that is described and analyzed in depth in this article.

In conclusion, none of the research works that have been analyzed have the same purpose as the one addressed in this paper, i.e. the alignment of digital models of individual teeth for typodont work. In this particular case, such alignment is required to carry out a comparative analysis of the digital models of preparations made on the same tooth model by different people with respect to a recipe or a master model, in order to evaluate their skills in the handling of subtractive rotary cutting tools (turbines, contra-angle hand-pieces, etc.).

The article is organized as follows. Section 2 provides an overview of the materials utilized in this work, including the dental material from which the teeth are crafted and the imaging scanner employed, along with the associated methodology. This methodology comprises the alignment of the base with the method developed ex professo, as well as the application of the deformable model for the periodic re-sampling of the point cloud resulting from the scan. Section 3 then presents the results of applying this methodology to three pairs of teeth with differentiating characteristics. Finally, Section 4 outlines the conclusions and intended future work.

## 2. Materials and method

### *2.1. Materials*

The teeth used in this work are made of Duroplastic®, a material that imitates dentine and is characterized by the fact that it does not generate solid residue when milled (see Fig. 1(a)). The digitization of the pieces is carried out using a desktop 3D dental scanner, specifically the Aidite® A-IS Pro, which is shown in Fig. 1(b) and Fig. 1(c). This equipment, which uses blue light technology (structured light), offers a precision of less than 10 microns and a resolution of 1.3 MP. For the digitization of the abutment-type preparations of the study. The time employed in this scan is approximately 13 seconds and the output format chosen is .STL because our interest is focused exclusively on the geometry of the object and not on its texture or color.

As can be seen in Fig. 1(c) the current scanning methodology with tabletop scanners in the laboratory uses a mobile platform that rotates the model to be scanned in the same order to cover all its surfaces. To ensure that the model does not move during the scanning process, it is usually placed with a clamping putty that keeps the model temporarily attached to the platform during scanning and prevents displacement or the model from falling. This methodology has a number of limitations:

- Imperfect attachment of the model to the scanning platform due to the mechanical and holding properties of the clamping putty.

- Impossibility of obtaining identical 3D models of the same model due to the possible movement of the model during scanning (distortion) and differences in the modeling of the putty itself which will be scanned at the same time as the model to be scanned.
- Impossibility to scan the base of a model or parts of the model that are immersed in the putty.
- Only complete models can be scanned and not single teeth without burying part of the root (as well as having sufficient retention against model movement).
- The same model cannot be scanned multiple times without altering its initial scanning position if it is removed from the scanning platform between scans, therefore the alignment of the models is limited to the alignment capability and accuracy of the post-processing methodology.


(a) (b) (c)

Figure 1: (a) Virgin canine n.36, (b) Aidite A-IS Pro scanning in horizontal position, (c) scanning in vertical position.

In an attempt to alleviate some of these issues, a special base has been developed to fix the two elements to be scanned. The lower part is fixed to the base of the scanner by means of an adhesive material, and as can be seen in the left-hand part of Fig. 2(a), it has a customized indentation into which the upper base fits. On the other hand, the right-hand part of Fig. 2(a) shows an example of upper type base, which has an alveolus in their center on which the stem of the tooth to be scanned is fitted and screwed. In this way, the lower base is universal, while the upper base varies depending on the dental piece to be scanned. At the same time, to facilitate the alignment between scans, the geometry of the fitting system between the parts consists of notches with different widths that serve as references. An example of both elements coupled with a bolt-on tooth can be seen in Fig. 2(b).

Due to the screwing/unscrewing of teeth with the dynamometric spanner (see Fig. 2(c)) and fitting/unfitting of lower and upper elements for the scanning of successive dental pieces, the material must guarantee chemical resistance, durability, and excellent formability for manufacturing purposes. After different material tests, the scanning elements are finally manufactured with a Prusa MK3 S2+ printer using PETG (PolyEthylene Terephthalate Glycol) filament which offers a good trade-off between cost and the desired durability.

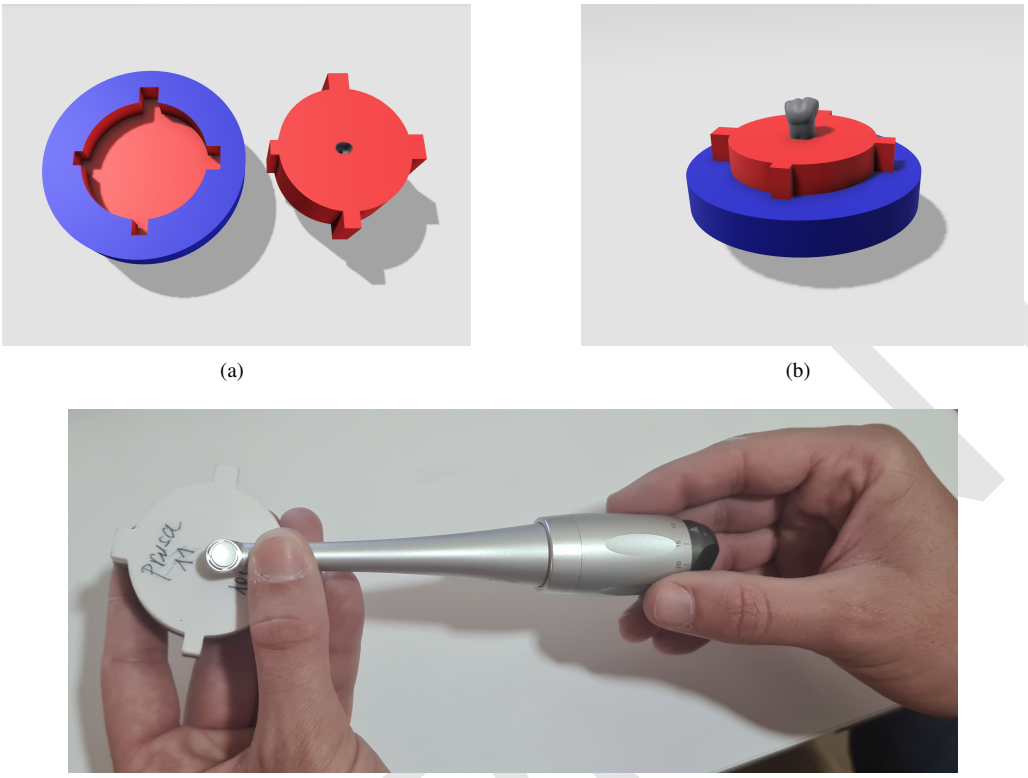

(a) (b)

(c)

Figure 2: (a) Separate lower and upper elements of the reference base, (b) assembled elements with bolted tooth, (c) screwing the tooth with a dynamometric spanner.

### 2.2. Methodology

This section thoroughly describes the mathematical background needed to compare 3D-scanned dental pieces. The method involves three distinct stages. The first stage aligns the 3D point cloud using the reference base described in Section 2.1 and shown in Fig. 2(a). After properly aligning the reference base, the point cloud corresponding to the tooth is segmented. Then, a precise alignment of the dental piece is performed. In the second stage, a parametric deformable model is applied to the point cloud of the tooth to transform the non-periodic sampled point cloud into a continuous and regular mesh. This allows for accurate and efficient comparison between different scans, which constitutes the third stage of the proposed method. Note that the proposed approach is designed specifically for the comparison of 3D scan of dental pieces, as described in Section 1.

#### 2.2.1. Base alignment

Let us denote $\mathbf{p} = \langle \mathbf{x}, \mathbf{y}, \mathbf{z} \rangle$ as the $i$ points in the point cloud resulting from the 3D scan, where $\mathbf{x} = \{x_i\}, \mathbf{y} = \{y_i\}, \mathbf{z} = \{z_i\}$ are the Cartesian coordinates. Approximately 97% of the $i$ points correspond to the reference base, while the remaining 3% correspond to the tooth. Therefore, the points corresponding to the reference base provide sufficient information for the alignment process. Fig. 3 shows the rendering of the aforementioned point cloud.

Firstly, it is necessary to calibrate the displacement in the $XY$ plane of the 3D scan. It is important to note that the reference base is cylindrical and its symmetry axis should correspond to the location of the tooth. This requires calculating the center of mass of the point cloud and applying an offset to the $x$- and $y$-axes to compensate for any misalignment of the 3D model as shown in Eq. 1,

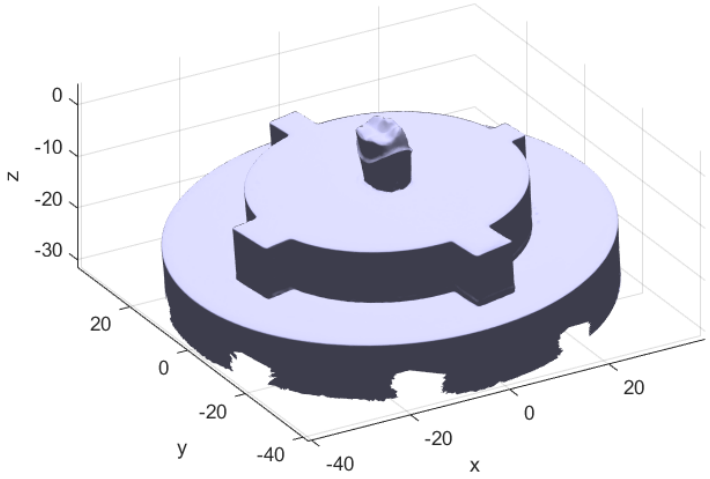


Figure 3: Render of the point cloud from the 3D scan of the reference base and the tooth before the alignment process.

$$\begin{aligned} x_i &= x_i - \bar{x}_i, \\ y_i &= y_i - \bar{y}_i, \end{aligned} \tag{1}$$

where $x_i \in \mathbf{x}$ and $y_i \in \mathbf{y}$ are the $x$- and $y$-coordinates of the $i$-th point of the point cloud $\mathbf{p} = \langle \mathbf{x}, \mathbf{y}, \mathbf{z} \rangle$. $\bar{x}_i$ and $\bar{y}_i$ are the average of the coordinates $x_i$ and $y_i$ respectively, i.e., the center of mass of the point cloud with respect to the $XY$ plane. The result of applying the $XY$ alignment is shown in Fig. 4.

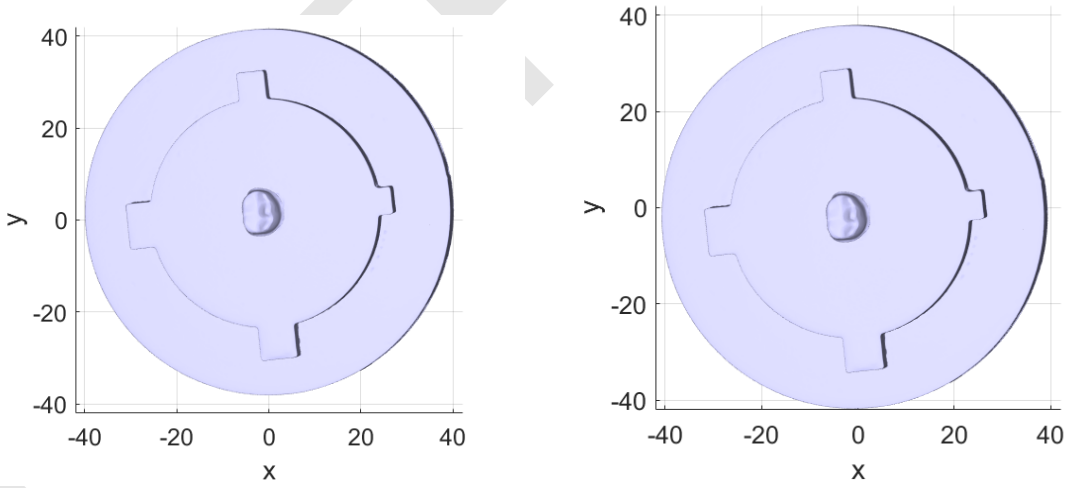


Figure 4: Render of the point cloud from the 3D scan (a) before and (b) after the $XY$ alignment.

The next step is to correct the inclination of the reference base. As shown in Fig. 3 - Fig. 4, the reference base has two planes that are suitable for this purpose. A disc is located on the upper plane, around the tooth insertion site, while an annulus on the bottom plane separates the two cylindrical elements of the base. It has been empirically verified, using various 3D models in the database, that the upper disc is the most optimal plane for adjusting the base.

Therefore, the points defining this upper disc will be used as the reference data for this step.

To select the points corresponding to the upper disc, the $z$-coordinate of all points is used to calculate its histogram. An accuracy of one hundredth of a millimeter for the discretization of the $z$-axis is considered optimal. The histogram analysis enables us to select the points corresponding to the upper disc using a statistical procedure. The histogram in Fig. 5(a) shows two maxima corresponding to the two reference planes where most of the points are located. In order to select the interval of $z$ values around the maximum corresponding to the upper disc, a threshold of 25% above the histogram maximum is applied. Note that if the base tilt is significant, the statistical dispersion will be high. This may cause gaps to appear in the histogram, which can affect the result. To address this issue, a 1D morphological process is applied before the selection, which involves a closing followed by an opening operation [27].

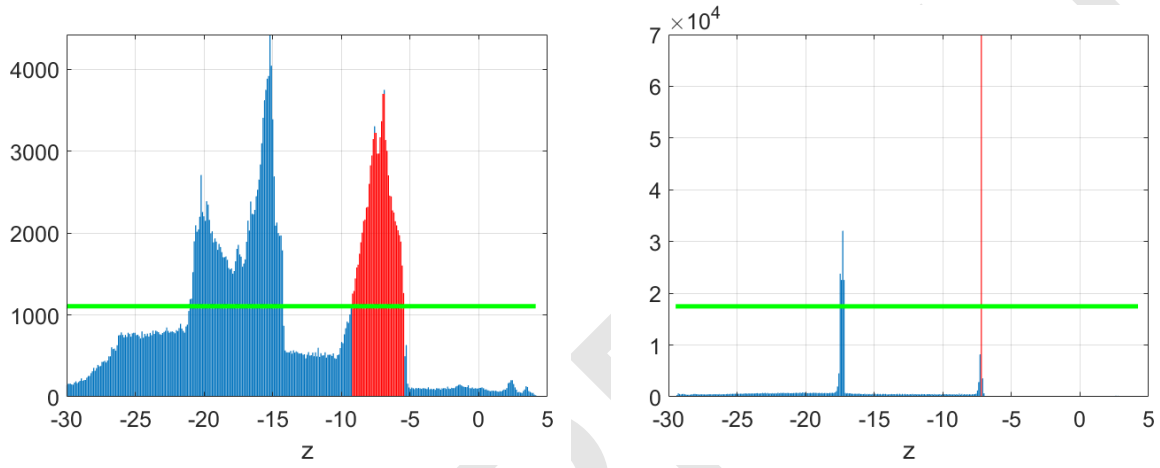


(a) (b)

Figure 5: (a) Histogram of the $z$-coordinate of the points before the correction of the reference base inclination. The red bars correspond to the $z$ interval whose values are selected as the upper disc. (b) Histogram of the $z$-coordinate of the points after the correction.

Next, the points whose $z$-coordinate meets the criterion defined by the histogram are selected as the point set $\mathbf{p}_{ua}$. From these points, those $\mathbf{p}_{ua}$ that satisfy $\rho_{min} < \rho_i < \rho_{max}$ are selected, where $\rho_i$ is the radial coordinate of each point $i$ expressed in polar coordinates. The values $\rho_{min}$ and $\rho_{max}$ represent the radius of the tooth insertion location and the radius of the upper disc, respectively. Therefore, $\mathbf{p}_{ua}$ represents the points on the upper annulus, which are shown in red in Fig. 6.

Then, the least squares method [28] is used to fit an Euclidean plane represented by the equation $ax + by + c = z$, to the set of points $\mathbf{p}_{ua}$. Matrix $A$ and arrays $\mathbf{d}$ and $\mathbf{z}_{ua}$ are defined as follows,

$$A = \begin{bmatrix} x_1 & y_1 & 1 \\ x_2 & y_2 & 1 \\ \vdots & \vdots & \vdots \\ x_n & y_n & 1 \end{bmatrix}, \quad \mathbf{d} = \begin{bmatrix} a \\ b \\ c \end{bmatrix}, \quad \mathbf{z}_{ua} = \begin{bmatrix} z_1 \\ z_2 \\ \vdots \\ z_n \end{bmatrix}, \tag{2}$$

where $x_i$, $y_i$ and $z_i$ correspond to the $x$-, $y$- and $z$-coordinates of the set of points $\mathbf{p}_{ua} = \langle \mathbf{x}_{ua}, \mathbf{y}_{ua}, \mathbf{z}_{ua} \rangle$. We define $\mathbf{A} = A^\top A$ and $\mathbf{e} = A^\top \mathbf{z}_{ua}$, where $A^\top$ denotes the transpose of $A$. The parameters of the plane $\mathbf{d} = [a, b, c]^\top$ can be easily obtained as

$$\mathbf{d} = \mathbf{A}^{-1}\mathbf{e}. \tag{3}$$

Fig. 6 shows the plane along with the set of points $\mathbf{p}_{ua}$, and the normal vector $\mathbf{u}_n$ to the plane. The normal vector can be calculated with $\mathbf{u}_n = [-a, -b, 1]$.

From the normal vector $\mathbf{u}_n$, the unit vector $\mathbf{u}_a$ is derived as

$$\mathbf{u}_a = \frac{1}{\sqrt{u_{nx}^2 + u_{ny}^2}} \begin{bmatrix} u_{ny} & -u_{nx} & 0, \end{bmatrix} \tag{4}$$

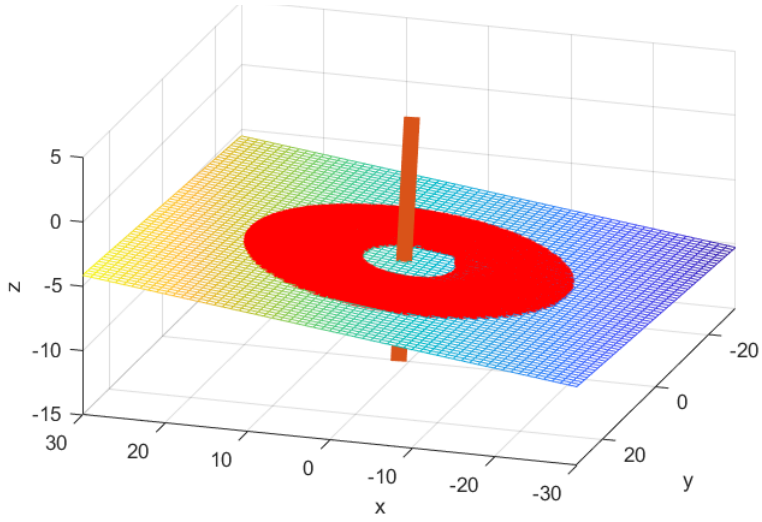


Figure 6: Correction of tilt using least squares adjustment. The points corresponding to the upper annulus, $\mathbf{p}_{ua}$, are depicted in red and the resulting plane is plotted with a mesh. The line represents the normal vector $\mathbf{u}_n$ to the resulting plane.

which is used as the rotation axis of the model. The vector $\mathbf{u}_n$ can be expressed in spherical coordinates, $\mathbf{u}_n = [r, \phi, \theta]$, where $r$, $\phi$ and $\theta$ represent the radial line, the polar angle and the azimuthal angle, respectively. Then, the rotation matrix $R_1$, which allows rotation from the axis $\mathbf{u}_a = [u_{ax}, u_{ay}, 0]$ and the angle $\alpha$, is defined as

$$R_1 = \begin{bmatrix} \cos\alpha + u_{ax}^2(1-\cos\alpha) & u_{ax}u_{ay}(1-\cos\alpha) & u_{ay}\sin\alpha \\ u_{ay}u_{ax}(1-\cos\alpha) & \cos\alpha + u_{ay}^2(1-\cos\alpha) & -u_{ax}\sin\alpha \\ -u_{ay}\sin\alpha & u_{ax}\sin\alpha & \cos\alpha \end{bmatrix}, \tag{5}$$

where $\alpha = \pi/2 - \theta$. This matrix is applied to the point cloud,

$$\mathbf{p}_1 = R_1\mathbf{p}, \tag{6}$$

where $\mathbf{p}_1 = \langle \mathbf{x}_1, \mathbf{y}_1, \mathbf{z}_1 \rangle$ stands for the point cloud after applying the rotation. Fig. 7 illustrates the relevant vectors and angles involved in the rotation process.

To ensure the inclination adjustment of the reference base a second analysis based of the histogram of the $z$-coordinate of $\mathbf{p}_1$ is applied. As can be seen in the histogram shown in Fig. 5(b), the tilt of the reference base has been corrected since most points on the upper annulus are now at the same $z$-coordinate. The maximum of the histogram determines the reference for the vertical offset $z_{of}$,

$$\mathbf{p}_2 = \left\langle \mathbf{x}_1, \mathbf{y}_1, \mathbf{z}_1 - z_{of} \right\rangle, \tag{7}$$

where $\mathbf{p}_2$ represents the point cloud after this adjustment. Fig. 8 illustrates the rendering of the point cloud before and after the rotation and vertical shift corrections.

The next stage in the method is to align the polar angle $\phi$ of the reference base points using the $z$-axis as the axis of rotation. This is achieved by determining the rotation angle of the base points using the lateral fins of the structural frame as a reference. Fig. 4 depicts a 3D azimuthal view of the base, where the lateral fins are clearly visible. In the following step, the lateral fins will be aligned with the $XY$ plane.

The points located between the two annuli are referred to as $\mathbf{p}_{2c}$, see Fig. 9(a). Thereafter, a histogram is applied to the polar coordinate of $\mathbf{p}_{2c}$, allowing the radius of the reference base to be determined statistically. Subsequently, the points are segmented based on their radial distance from the centre of mass, resulting in the identification of those points belonging to the lateral fins, which are outlined in blue in Fig. 9(b).

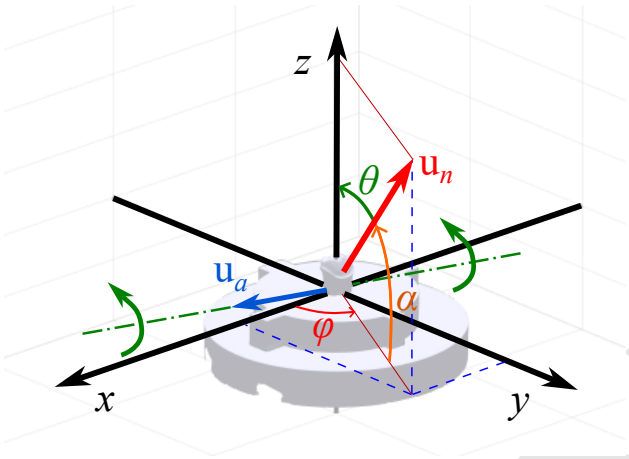


Figure 7: Schematic figure with the relevant vectors and angles involved in the rotation of the reference base. The normal vector to the plane of the base and the unit vector defining the axis of rotation are denoted as $\mathbf{u}_n$ and $\mathbf{u}_a$, respectively. The rotation applied to the structure is referred to as $\theta$.

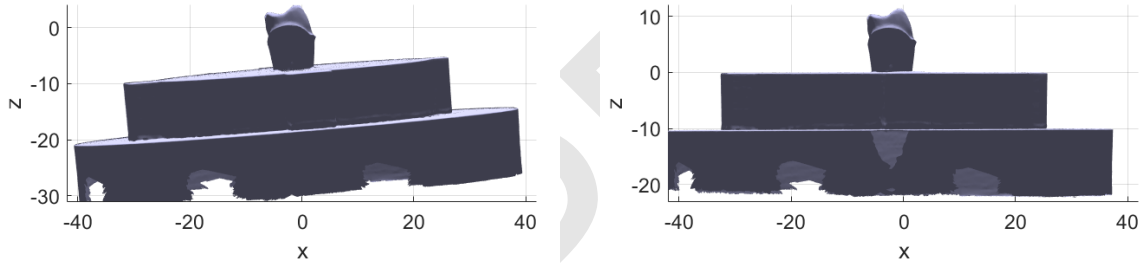


(a) (b)

Figure 8: Reference base (a) before and (b) after tilt and $z$-coordinate adjustment.

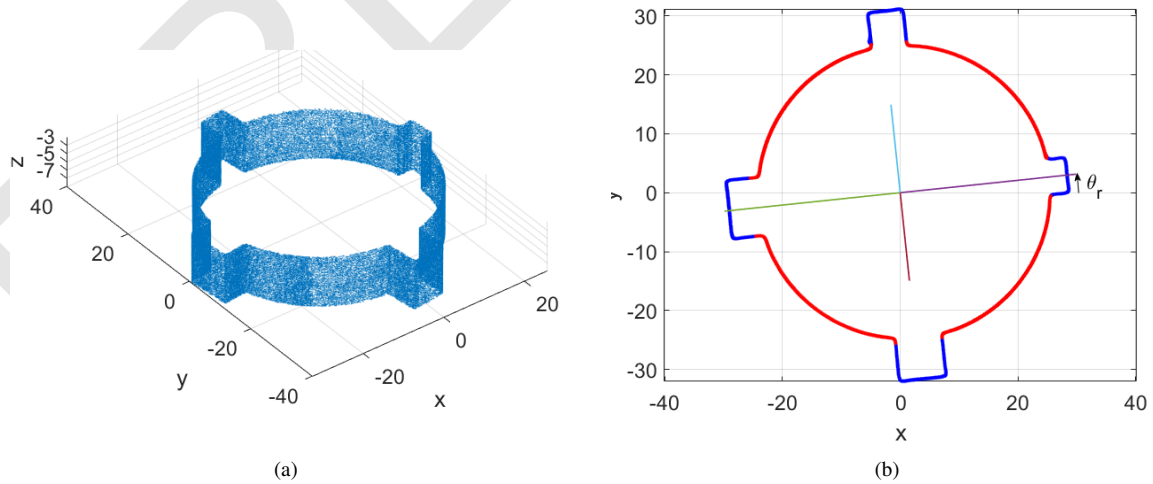


(a) (b)

Figure 9: (a) Set of points on the reference base located between the upper and lower annuli, (b) Azimuthal view of this set of points. The lines inside the structure show the angle of the lateral fins with respect to the $x$- and $y$-axes, calculated using the proposed method.

The $x$- and $y$-coordinates of the lateral fin points are projected in an azimuthal plane producing a binary image from which the Hough transform is calculated, as shown in Fig. 10. Since the lateral fins are parallel and perpendicular to each other, the maxima of the Hough transform can be used to determine the angle of the horizontal and vertical sides of the fins. This is illustrated in Fig. 10, where the maxima is marked with a white box. It is important to note that a maximum will always be obtained at a specific angle, $\theta_r$. This represents the parallel side of the fins and is accompanied by a second maximum at $\theta_r + \pi/2$, which represents the perpendicular side of the fins. The centre lines in Fig. 9(b) illustrate the $\theta_r$ angle calculated by this procedure, which is in alignment with the angle of the fin sides as depicted in the figure.

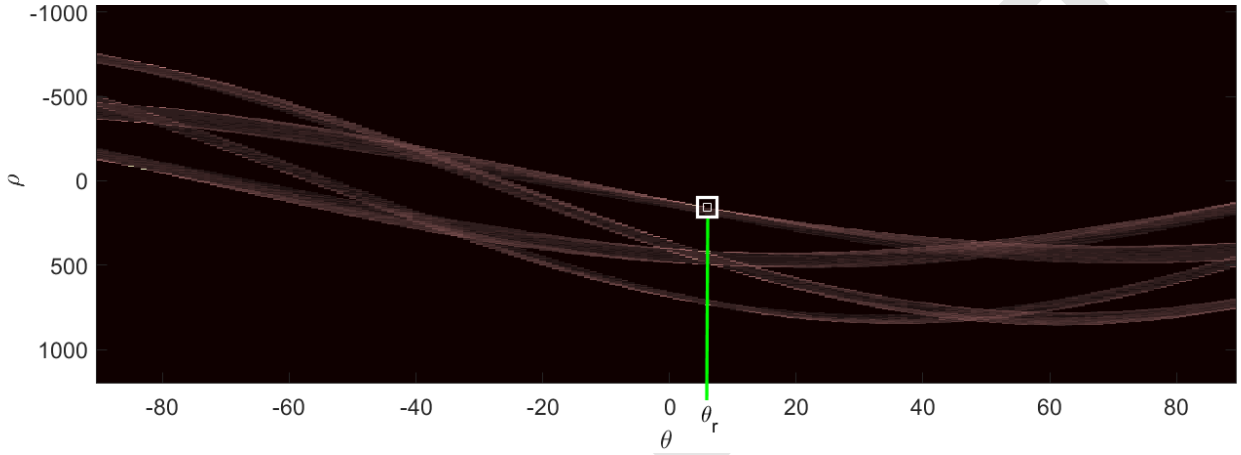


Figure 10: Hough transform of the binary image derived from the lateral fins of the reference base. The maximum of the Hough transform is marked by a white box, which allows the predominant angle $\theta_r$ in the fins to be obtained.

Once the angle $\theta_r$ has been determined, the point cloud is rotated in accordance with the following equation:

$$\mathbf{p}_3 = R_2 \mathbf{p}_2, \tag{8}$$

where $\mathbf{p}_2$ stands for the point cloud derived from Eq. 7 and $R_2$ represents the rotation matrix,

$$R_2 = \begin{bmatrix} \cos(-\theta_r) & -sin(-\theta_r) & 0 \\ sin(-\theta_r) & \cos(-\theta_r) & 0 \\ 0 & 0 & 1 \end{bmatrix}. \tag{9}$$

Once the rotation in the $z$-axis is corrected (see Fig. 11(a)), the final offset adjustment in the $x$ and $y$-axes may be implemented by using data provided by the lateral fins. Vertical misalignment is determined by using information from the horizontal fins, while horizontal misalignment is calculated based on the positional data from the upper and lower fins.

In order to identify the points corresponding to the fins located on the right and left, a histogram of the $x$-coordinate of the set of points located between the annulus, $\mathbf{p}_{3c}$, is constructed. To smooth out the narrow peaks, a low-pass filter based on 5-sample average window is applied. As can be observed in in Fig. 12(a), two groups of two peaks can be identified both on the right and on the left of the curve, which correspond to the vertical side walls and the beginning of the curved zone. By selecting the points whose $x$-coordinate is located within these peaks, we can identify the points corresponding to the horizontal fins. The red rectangles in the figure show the two intervals selected for the $x$-coordinate. A similar procedure can be employed to identify the upper and inner fins using the $y$-coordinate of the points, as illustrated in Fig. 12(b). The result of applying the offset correction in the $x$- and $y$-axes is presented in Fig. 11(b).

*2.2.2. Tooth segmentation and transformation into a 3D volume*

Once the reference base is fully aligned, as shown in Fig. 13, the tooth is segmented by selecting the subset of points above the coordinate $z = 0$ (see Fig. 14(a)). The point map of the tooth will be discretized and transformed

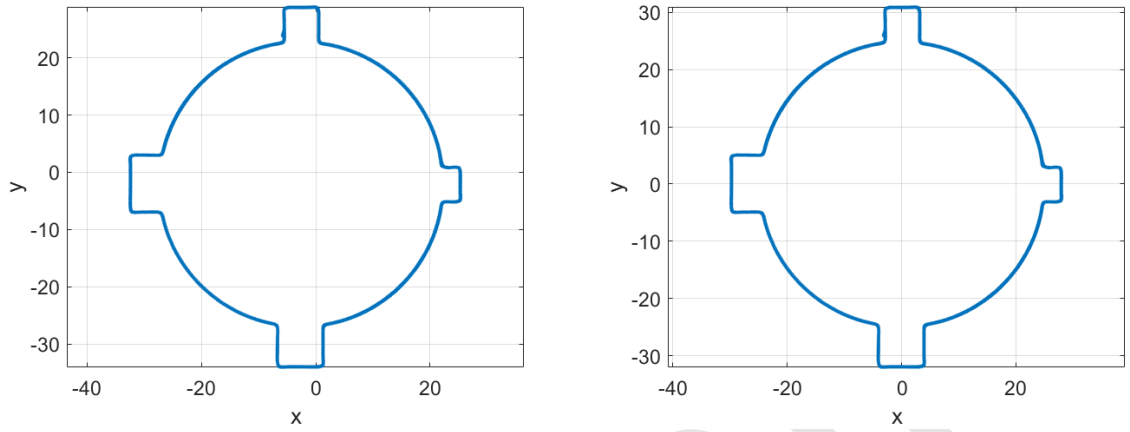


(a) (b)

Figure 11: Reference base (a) before and (b) after applying the offset in $XY$ plane.

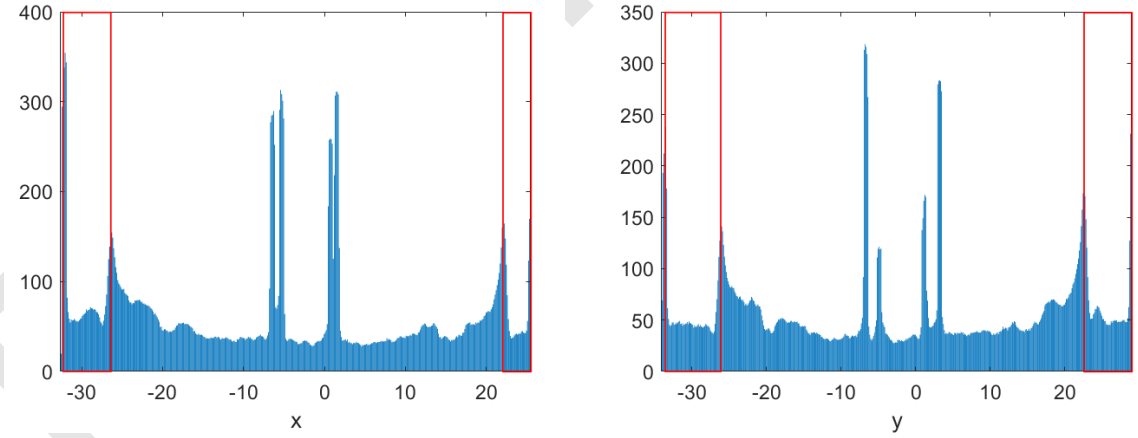


(a) (b)

Figure 12: Histogram of the (a) $x$-coordinate and (b) $y$-coordinate of the points of the central part of the reference base, $\mathbf{p}_{3c}$, low-pass filtered using a 5-sample sliding window. The red rectangles indicate the coordinates of the points corresponding to the fins.

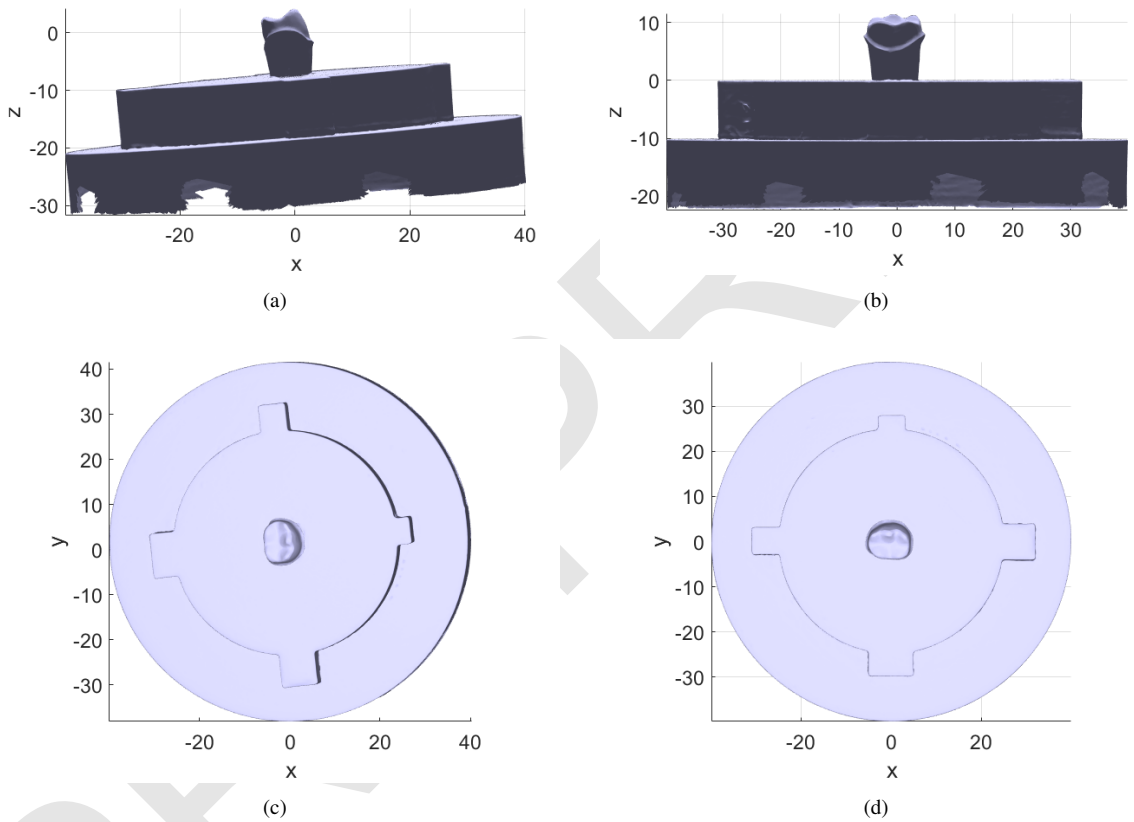


Figure 13: Lateral and azimuthal view of the reference base before (left-hand column) and after (right-hand column) the alignment process.

into a three-dimensional binary volume, which will be used to guide the deformable model. This transformation is achieved through the definition of a null binary volume to which each point of the cloud is assigned in a voxel with a single unit value, as illustrated in Fig. 14(b). Morphological processing [27] is employed to fill the interior of the voxels that define the tooth outline, thereby obtaining a three-dimensional mask, as illustrated in Fig. 14(c). Finally, the upper cap of this mask, depicted in Fig. 14(d), is selected as the base information for the application of the deformable model. Note that this data represents a discrete approximation of the upper part of the tooth, which will form the data set of interest in the AIDDA® system.

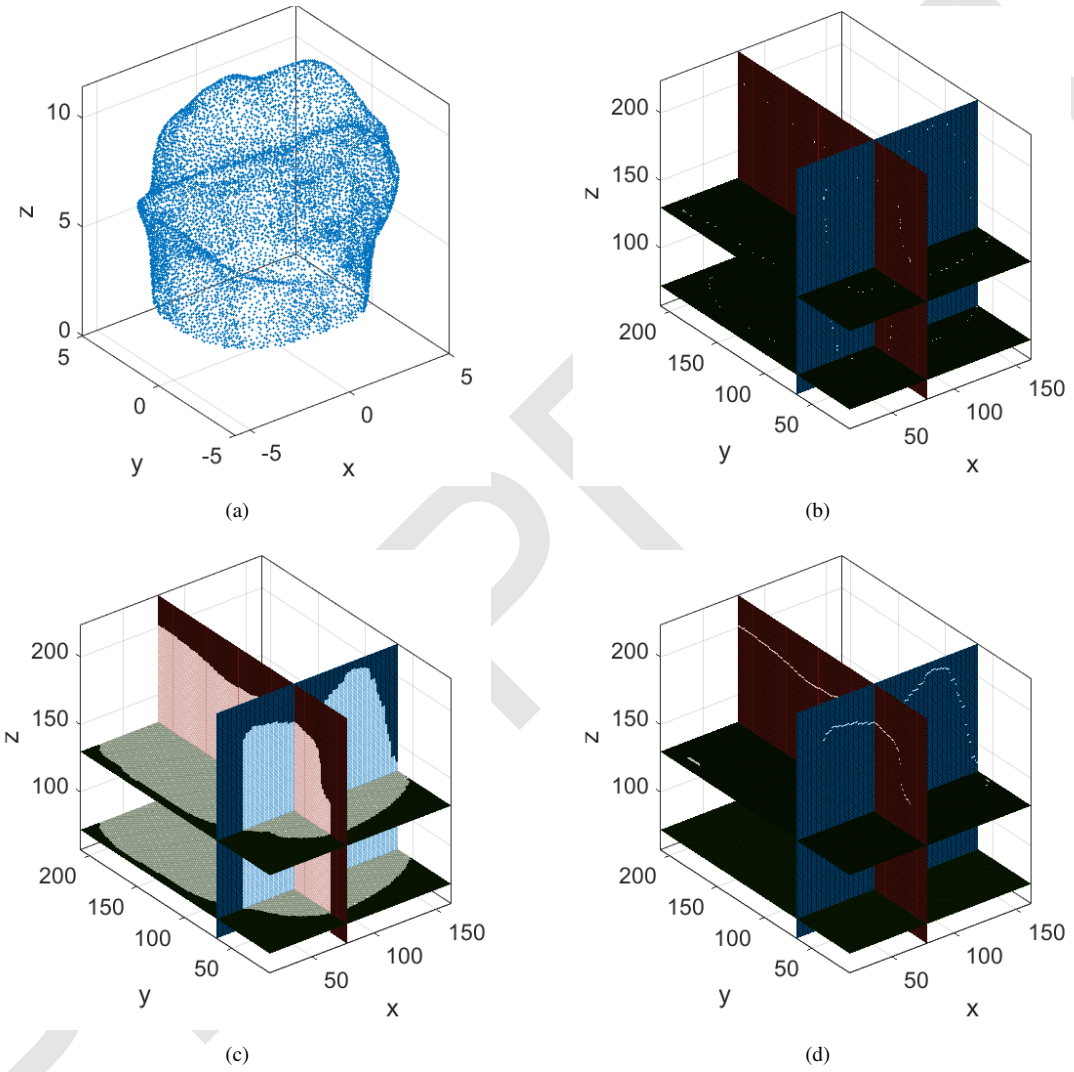


Figure 14: Transformation process of the point cloud into a binary 3D volume. (a) Point cloud corresponding to the tooth. (b) Transformation of the points into a binary 3D volume. (c) Point interpolation and filling of the tooth volume. (d) Segmentation of the upper part of the tooth volume.

### *2.2.3. Deformable model*

A deformable mathematical model is a three-dimensional structure capable of describing the boundaries of non-rigid physical objects [29, 30, 31], such as those represented by the teeth under analysis. The surface defined by the model deforms in response to internal and external forces. Internal forces emulate the physical characteristics required

for the object, such as surface smoothness. In contrast, external forces permit the model to be fitted to the specific shape of each individual tooth.

Deformable models are classified into explicit and implicit models [32, 33]. The explicit models, also referred to as parametric deformable models, are chosen for this work as they allow for the representation of the object by parametric surfaces. This facilitates the shape and position analysis, which is required in the teeth comparison. In the parametric models, external forces are a function of the gradient of the data, namely the binary data set shown in Fig. 14(d). Parametric models offer a multitude of approaches for formulating deformable models within the spatial domain. However, a frequency-domain formulation has been employed in this approach, since a lower computational complexity faster fitting to the data under analysis can be achieved [34, 35].

A 3D deformable model is a parametric surface in $\mathbb{R}^3$

$$\mathbf{v} := \mathbf{v}(\mathbf{s}, t) = [v_x(\mathbf{s}, t), v_y(\mathbf{s}, t), v_z(\mathbf{s}, t)]^\top, \tag{10}$$

where the variable $t$ represents the time, $v_i(\mathbf{s}, t)$ denotes the coordinate function for $x$, $y$ or $z$, and the spatial parametric variables are collected in $\mathbf{s} := [s_1, s_2]$, where $s_j \in [0, L_j]$ and $L_j$ denotes the length of the model in the direction of $j$. In this approach, the parametric variables will be aligned with the $x$- and $y$-axes, i.e., $s_1 = s_x$ and $s_2 = s_y$.

The behavior of the model is conditioned by a functional that incorporates both internal and external restrictions considered as energies, $\mathcal{E}(\mathbf{v}) = \mathcal{S}(\mathbf{v}) + \mathcal{P}(\mathbf{v})$. The first energy term, $\mathcal{S}(\mathbf{v})$, emulates the internal energy of deformation whereas the second term, $\mathcal{P}(\mathbf{v})$, is a external energy given by a potential function based on the gradient of the data. The minimization of this energy functional through an iterative process allows for the derivation of a mathematical representation of the tooth surface [29, 32].

The evolution of each component $v_i(\mathbf{s}, t)$ is calculated by the discretization of the spatial variables $\mathbf{s}$, resulting in the union of $N = N_1 \cdot N_2$ elements. Similarly, the time variable $t$ is also discretized using $t = \xi\Delta t$, $\Delta t$ being the temporal sampling period. Thus, the following iterative equation is derived,

$$\left(\left(\frac{m}{\Delta t^2} + \frac{c}{\Delta t}\right)\mathbf{F} + \mathbf{K}\right)\mathbf{u}_\xi = \left(\frac{2m}{\Delta t^2} + \frac{c}{\Delta t}\right)\mathbf{F}\mathbf{u}_{\xi-1} + \left(\frac{-m}{\Delta t^2}\right)\mathbf{F}\mathbf{u}_{\xi-\mathbf{2}} + \mathbf{q}_{\xi-1}. \tag{11}$$

where $\mathbf{u}_\xi$ are the nodal variables of the model at the time stamp $\xi$, $\mathbf{q}_\xi$ are the external forces for the same time $\xi$, $m$ is the mass and $c$ is the damping of the model. The matrices $\mathbf{F}$ and $\mathbf{K}$ can be calculated analytically for each shape function used in the spatial discretization [36].

Eq. 11 can be analyzed in the frequency domain by using the two-dimensional Fourier transform. Rearranging the resulting equation in the frequency domain we obtain,

$$U_\xi(\bar{\omega}) = H(\bar{\omega})\left(a_1 U_{\xi-1}(\bar{\omega}) + a_2\, U_{\xi-2}(\bar{\omega}) + \frac{Q_{\xi-1}(\bar{\omega})}{\eta F(\bar{\omega})}\right), \tag{12}$$

where $U(\bar{\omega})$, $F(\bar{\omega})$ and $Q(\bar{\omega})$ are the two-dimensional representations in the frequency domain of their respective spatial sequences, $\bar{\omega} := [\omega_1, \omega_2]$ is the vector of continuous frequency variables, $\eta = m/\Delta t^2 + c/\Delta t$, $\gamma = \Delta t\, c/m$, $a_1 = 1 + (1+\gamma)^{-1}$ and $a_2 = -(1+\gamma)^{-1}$. Further details can be found in [34, 35].

Eq. 12 represents the motion and behavior of the model in the adaptive iterative process of characterizing the data. The two-dimensional filter $H(\bar{\omega}) = 1/(1 + K(\bar{\omega})/\eta F(\bar{\omega}))$, as detailed in [36], is employed to impose internal forces, while external forces are applied by means of $Q(\bar{\omega})$. The component $Q$ is calculated by applying a gradient in the $z$-direction to a Gaussian-filtered version of the data volume extracted from the tooth. This facilitates a gradual adaptation of the model to the border of the three-dimensional data.

In this approach, a two-dimensional deformable model is defined as a three-dimensional mesh. The coordinate functions $v_x$ and $v_y$ are initialized as an equally spaced mesh and are kept invariant. Eq. 12 is then applied to the coordinate function $v_z$, allowing for adaptation to the tooth surface. Fig. 15 presents a diagram of the model prior to the adaptation process. Table 1 gathers a brief description of the parameters and their values. As illustrated in the table, the tooth surface is characterized by the model using a $256 \times 256$ node mesh, which represents a compromise between precision and computational efficiency. The remaining parameters are selected to optimize the fit for three-dimensional dental data. It should be noted that the $\gamma$ parameter, which regulates the adjustment speed in relation to its precision, is calculated using an optimization algorithm defined in [37, 38].

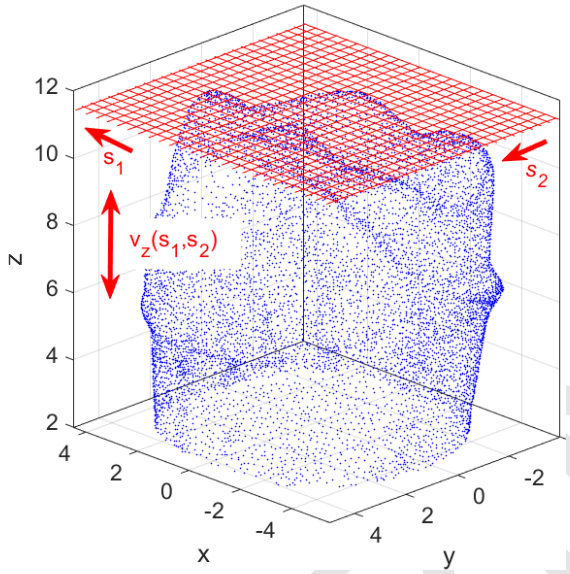


Figure 15: Scheme of the deformation model applied to the tooth. Deformable model depicted as a mesh in red. The $v_x$ and $v_x$ coordinate function of the nodes remain unchanged, while the $v_z$ coordinate function is modified by Eq. 12 in order to adapt to the upper surface of the tooth. The parametric variables $s_1$ and $s_2$ are aligned with the $x$- and $y$-axes.

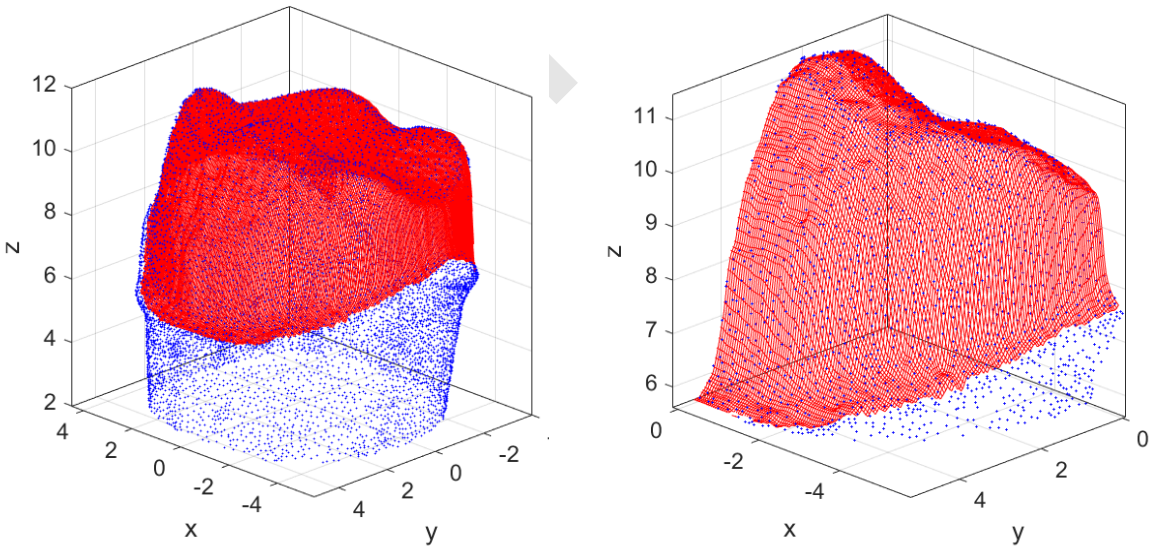


(a) (b)

Figure 16: Fitting of the deformable model to the upper part of the point cloud. The points are shown in blue +, while the deformable model is shown as a mesh in red. (a) Full view of the complete tooth. (b) Zoom detail.

| Parameter | Value | Description |
|---|---|---|
| Shape function | Finite differences | Function used in the spatial discretization of the model |
| $N_1 \times N_2$ | $256 \times 256$ | Number of nodes of the model |
| $N_{1h} \times N_{2h}$ | $256 \times 256$ | Number of hidden nodes of the model |
| $\alpha$ | 0.25 | Elasticity of the model |
| $\beta$ | 1.5 | Rigidity of the model |
| $\eta$ | 1.0 | Equivalent mass |
| $\gamma$ | $\gamma_o$ (optimal) | Damping-mass ratio |
| $N_s$ | 49 | Gaussian filter impulse response length |
| $f_{ext}$ | 20 | Multiplicative factor for the external forces |
| $iter_{max}$ | 250 | Maximum number of iterations |

Table 1: List of the parameters and values used in the deformable model.

Fig. 16 illustrates the outcome of applying the deformable model to the point cloud of the tooth. As can be observed in the graphic, the resulting three-dimensional mesh allows the tooth surface to be characterized in a completely regular manner by means of the parametric surface $\mathbf{v}$, thereby enabling the subsequent comparison between teeth as required in the AIDDA® system.

## 3. Results

In order to validate the proposed approach, two different types of teeth produced by the manufacturer Frasaco® have been analyzed in terms of their morphology. On one hand, the teeth labeled D1 and D2 correspond to molar tooth no. 36 of dentition type AG-3. Both teeth have been carved using rotary cutting tools by two accredited professionals in accordance with the specifications set forth by the manufacturer, Ivoclar®. In the case of the D1 model, the professionals employed a contra-angle hand-piece as the tool for the procedure. In contrast, a turbine tool was employed for the D2 model. Both D1 and D2 teeth has been scanned twice consecutively using the device described in Section 2.1. For each scan, the teeth were screwed and unscrewed from the reference base using a dynamometric spanner with a controlled torque of 15 nm. Fig. 17 depicts the D1 tooth before and after the carving process. On the other hand, tooth D3 is an uncarved, virgin tooth of the canine type, specifically tooth no. 13 of the AG-3 dentition type. The distinction between the two D3 scans is attributable to the torque employed for affixing them to the reference base, which was accomplished using a torque spanner of 10 and 20 nm, respectively. The resulting point clouds from the scanned D1, D2 and D3 are shown in Fig. 19, Fig. 22 and Fig. 25, respectively.

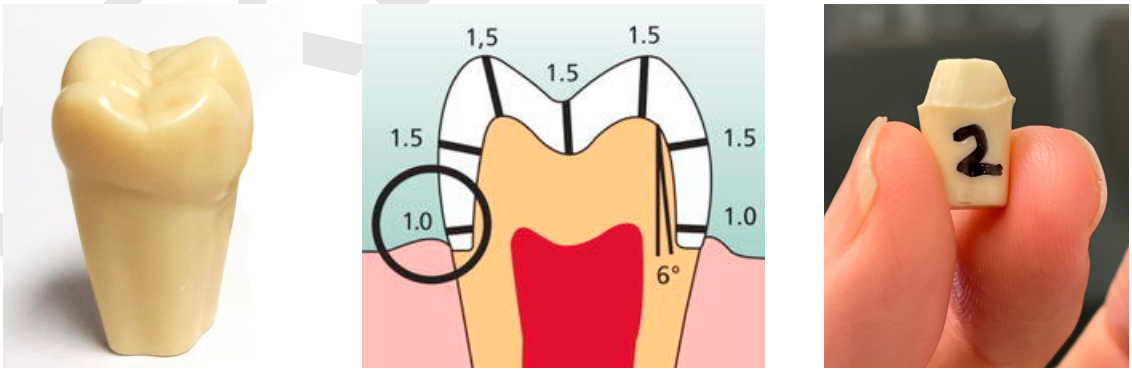


(a) (b) (c)

Figure 17: (a) Molar tooth no. 36, (b) Ivoclar® crown guide, (c) molar n. 36 carved according to the guide.

As illustrated in the figures, the resulting pair of point clouds for each tooth exhibits a discrepancy due to two factors: firstly, the non-periodic sampling of the scanner, and secondly, the variation in the initial positions of the reference base. Nonetheless, the resulting meshes of the deformable model have been aligned with the point clouds, thereby enabling an accurate comparison of each tooth scan with the others. Since there are two scans of the same tooth, this analysis allows to prove and calibrate that the proposed alignment and modeling is able to compensate the inaccuracies and misalignments that could be introduced by the scanning procedure.

Once the deformable model is applied to the aligned point cloud of each scanned tooth, a subtraction is performed between the $z$-coordinates of the deformable model, i.e. $v_z^{\mathtt{D}} = v_z^{\mathtt{A}} - v_z^{\mathtt{B}}$. This error matrix represents the discrepancy between the two teeth A and B, given by the distance along the $z$-axis between the nodes of the deformable models, which are aligned with each of the two teeth. However, as illustrated in Fig. 18(a), which depicts a slice detail of a pair of aligned teeth, the objective is to determine the distance in the normal direction between the two teeth, $v_z^{\mathtt{D}'}$, indicated by the dashed arrow in the illustration.

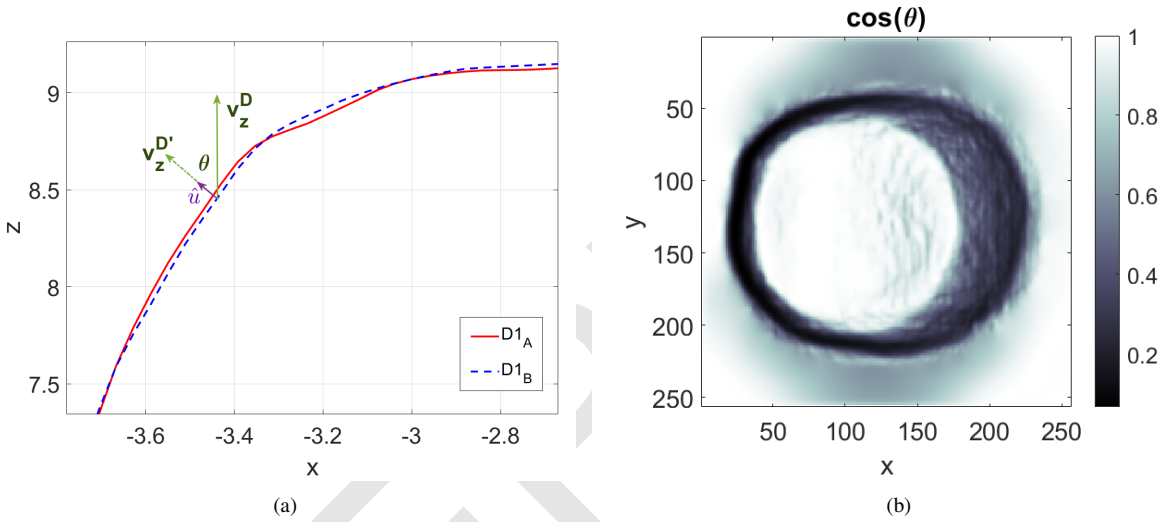


Figure 18: (a) Diagram for $\theta$ angle calculation. (b) Cosine of the $\theta$ angle for each node of tooth D1.

In order to obtain the desired error metric, the angle $\theta$ is computed at each node of the models, defined as the angle between the unit vector normal to each node, $\hat{u}_{n_1,n_2}$ and the $z$-axis. For each node of the deformable model with coordinates $n_1$ and $n_2$, the $x$-gradient,

$$\frac{\partial \bar{v}_z(n_1,n_2)}{\partial x} = \frac{\bar{v}_z(n_1+1,n_2) - \bar{v}_z(n_1-1,n_2)}{2\Delta x}, \tag{13}$$

and $y$-gradient are calculated,

$$\frac{\partial \bar{v}_z(n_1,n_2)}{\partial y} = \frac{\bar{v}_z(n_1,n_2+1) - \bar{v}_z(n_1,n_2-1)}{2\Delta y}, \tag{14}$$

where $\bar{v}_z(n_1,n_2) = \frac{1}{2}\left(v_z^{\mathtt{A}}(n_1,n_2) + v_z^{\mathtt{B}}(n_1,n_2)\right)$ is calculated as the mean value of the nodes of both models A and B and $\Delta x$ and $\Delta y$ represent the distance between nodes in the $x$- and $y$-directions, respectively. From the gradients, the normal vector to each node $\hat{u}_{n_1,n_2}$ is derived,

$$\hat{u}_{n_1,n_2} = \frac{\left(-\frac{\partial \bar{v}_z}{\partial x}, -\frac{\partial \bar{v}_z}{\partial y}, 1\right)}{\sqrt{\left(\frac{\partial \bar{v}_z}{\partial x}\right)^2 + \left(\frac{\partial \bar{v}_z}{\partial y}\right)^2 + 1}}. \tag{15}$$

The final step in the process is the calculation of the cosine of the angle $\theta$, which is determined by the dot product

between the vectors $\hat{u}_{n_1,n_2}$ and the unitary vector in the $z$-axis $\hat{u}_z$,

$$\cos(\theta) = \hat{u}_{n_1,n_2} \cdot (0,0,1) = \frac{1}{\sqrt{\left(\frac{\partial \bar{v}_z}{\partial x}\right)^2 + \left(\frac{\partial \bar{v}_z}{\partial y}\right)^2 + 1}}. \tag{16}$$

Fig. 18(b) illustrates the value of $\cos(\theta)$ for each node of the deformable models. This angle allows for the calculation of the error between the models in a direction normal to each node,

$$v_z^{\mathsf{D}'} = v_z^{\mathsf{D}} \cdot \cos(\theta). \tag{17}$$

Fig. 20, Fig. 23 and Fig. 26 show these differences $v_z^{\mathsf{D}'}$ for teeth D1, D2 and D3, respectively, both as a color map and as a three-dimensional drawing. The values shown on the color bar and on the axes are measured in millimeters (mm).

To graphically illustrate the fit between the two aligned scans of each tooth, Fig. 21, Fig. 24 and Fig. 27 show slices in the $x$- and $y$-directions of the deformable models applied to the three pairs of scans. Note that this visualization is possible since the deformable model provides a uniform mesh in both $x$- and $y$-axis. These figures show both the $z$-coordinate representation of the two scans A and B of the tooth and the difference between them. As can be seen, these differences are limited over most of the surface in the range $[-0.1, 0.1]$ mm.

Table 2 gathers the statistics calculated from the error matrix $v_z^{\mathsf{D}'}$: mean, standard deviation, mean square error (MSE), median absolute deviation (MAD) and the minimum and maximum values of this error matrix.

| Tooth | Mean and std. deviation | MSE | MAD | Min | Max |
|---|---|---|---|---|---|
| D1 | $+0.0165 \pm 0.0192$ | 0.00064 | 0.0205 | $-0.0576$ | 0.1179 |
| D2 | $-0.0055 \pm 0.0200$ | 0.00043 | 0.0158 | $-0.1110$ | 0.0979 |
| D3 | $+0.0124 \pm 0.0337$ | 0.00130 | 0.0293 | $-0.0933$ | 0.1416 |

Table 2: Statistics of the comparison between aligned teeth. The values are expressed in millimeters.

## 4. Discussion and conclusion

This work describes a novel approach for comparing scans of dental pieces. The proposed method comprises an alignment process and subsequent modeling through the use of an active mesh or parametric deformable model. To assess the accuracy of the proposed approach, three teeth, D1, D2 and D3 have been analyzed. Each teeth was scanned twice using a 3D scanner, resulting in two point clouds. Since some comparisons involve two scans of the same tooth, the two models generated through the proposed process provide a calibration and minimum error threshold of the scanning, alignment and subsequent modeling.

Two issues emerge during the scanning procedure. Firstly, there are physical limitations associated to the screwing of the tooth to the reference base and the fixing of the base to the scanner. The small size of the components introduces a significant challenge in the scanning process, given that minor discrepancies in the positioning of the teeth or the reference base can result in significant misalignment. Secondly, the non-periodic sampling of the scan introduces further difficulties when comparing two different point clouds. This can lead to difficulties in identifying potential areas of the tooth where carving defects may be present. These issues are intended to be compensated by the proposed alignment and modeling procedure.

Fig. 21, Fig. 24 and Fig. 27 illustrate that the difference between the slices of the model is less than 0.1 mm at any given point, which is a relatively minor discrepancy. Conversely, an examination of Fig. 19, Fig. 22 and Fig. 25 reveals that the model exhibits a high degree of alignment with the surface of the tooth. This is evidenced by the uniform distribution of maximum error values across the entire surface of the tooth, which reflects the effective adaptation of the deformable model to the surface defined by the point cloud.

In order to conduct an analytical assessment of the experimental outcomes, it is essential to examine the data presented in Table 2. As can be seen in this table, the mean values between 0.0055 mm and 0.0165 mm indicate that, on average, the models adapted to the point clouds are highly similar to one another. This can also be observed by comparing the mean square value and the absolute mean value, since in the least favorable case, tooth D3, these values

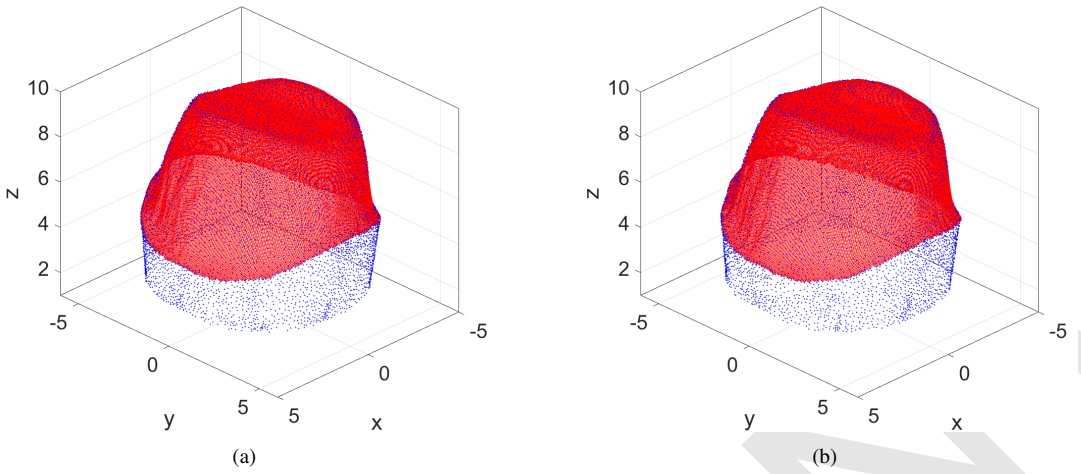


Figure 19: Result of the alignment and application of the deformable model to teeth (a) $\mathtt{D1_A}$ and (b) $\mathtt{D1_B}$.

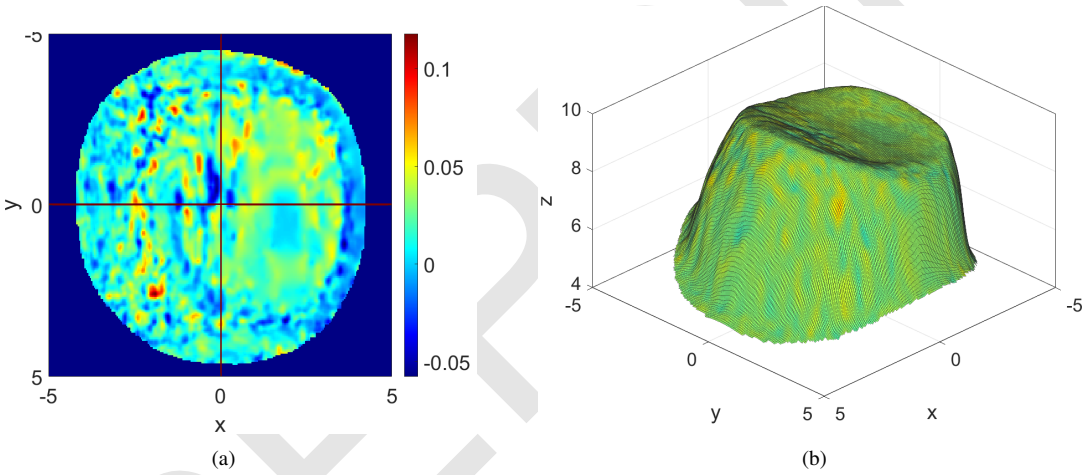


Figure 20: (a) Color map of the difference $v_z^{\mathtt{D1'}}$ and (b) 3D view. Values measured in mm.

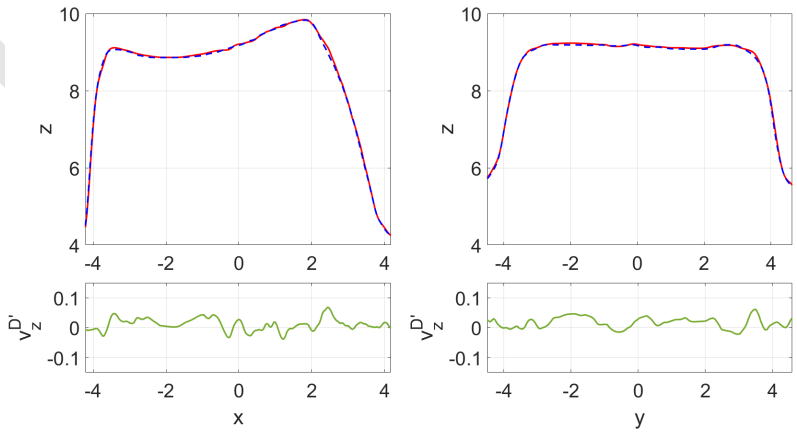


Figure 21: Top row shows slices of the teeth $\mathtt{D1_A}$ (solid red line) and $\mathtt{D1_B}$ (dashed blue line) whereas the bottom row shows $v_z^{\mathtt{D1'}}$. Left and right columns show the slices $y = 0$ and $x = 0$, respectively.

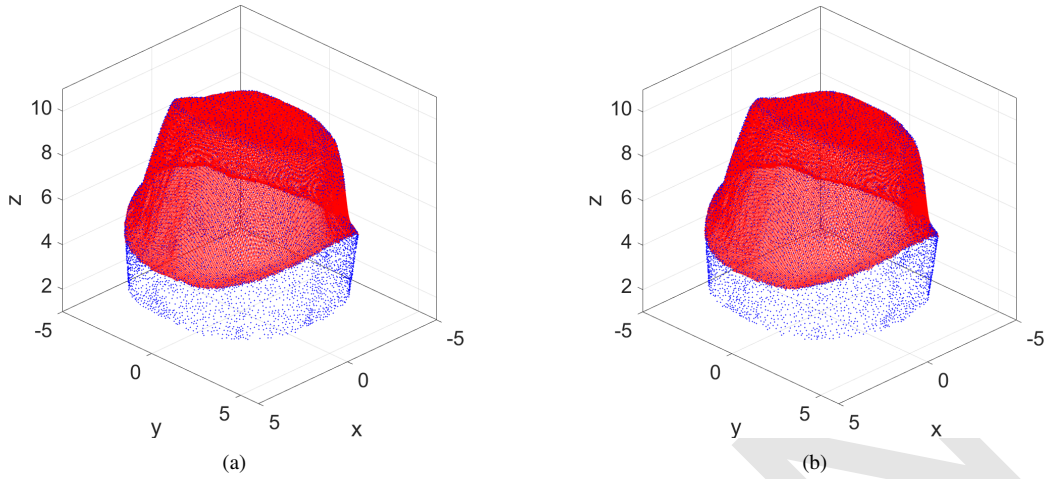


Figure 22: Result of the alignment and application of the deformable model to teeth (a) $\mathsf{D2}_{\mathtt{A}}$ and (b) $\mathsf{D2}_{\mathtt{B}}$.

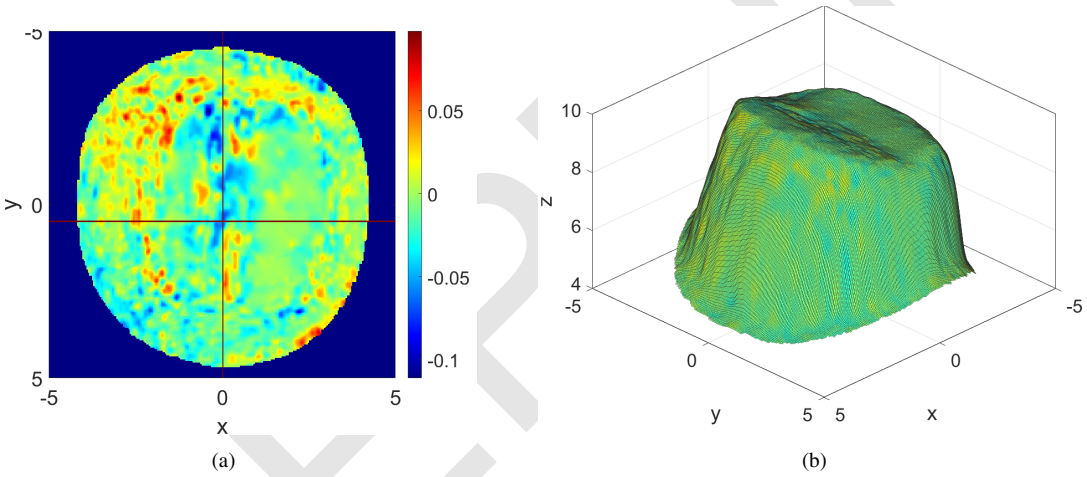


Figure 23: (a) Color map of the difference $v_z^{\mathsf{D2}'}$ and (b) 3D view. Values measured in mm.

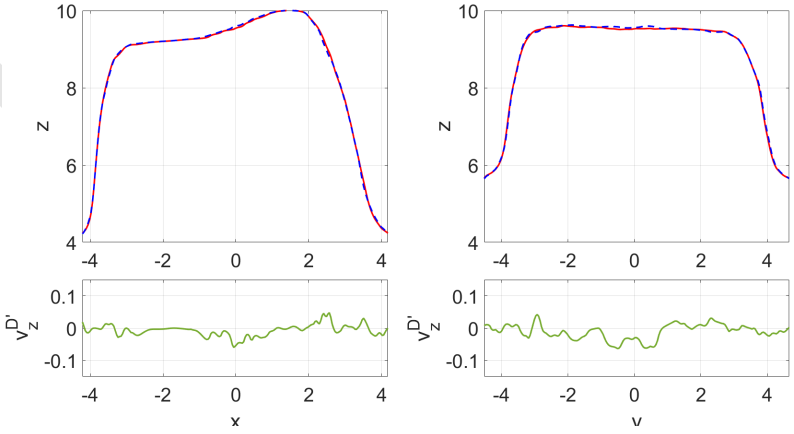


Figure 24: Top row shows slices of the teeth $\mathsf{D2}_{\mathtt{A}}$ (solid red line) and $\mathsf{D2}_{\mathtt{B}}$ (dashed blue line) whereas the bottom row shows $v_z^{\mathsf{D2}'}$. Left and right columns show the slices $y = 0$ and $x = 0$, respectively.

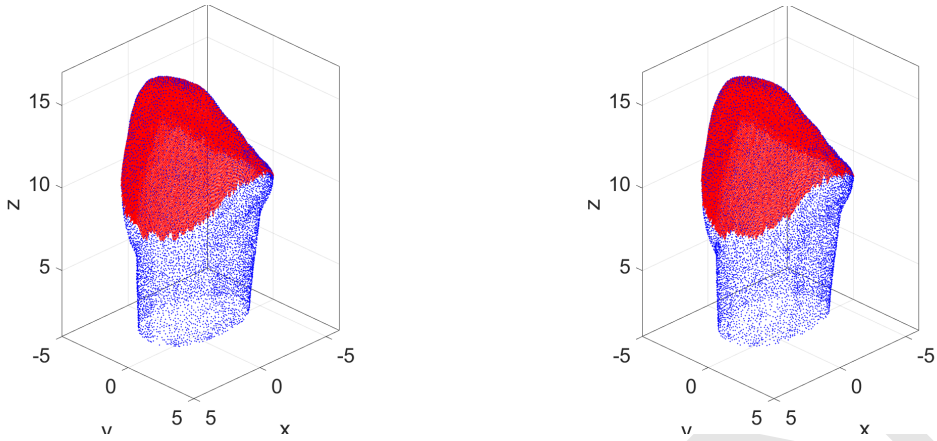


Figure 25: Result of the alignment and application of the deformable model to teeth (a) $\mathsf{D3_A}$ and (b) $\mathsf{D3_B}$.

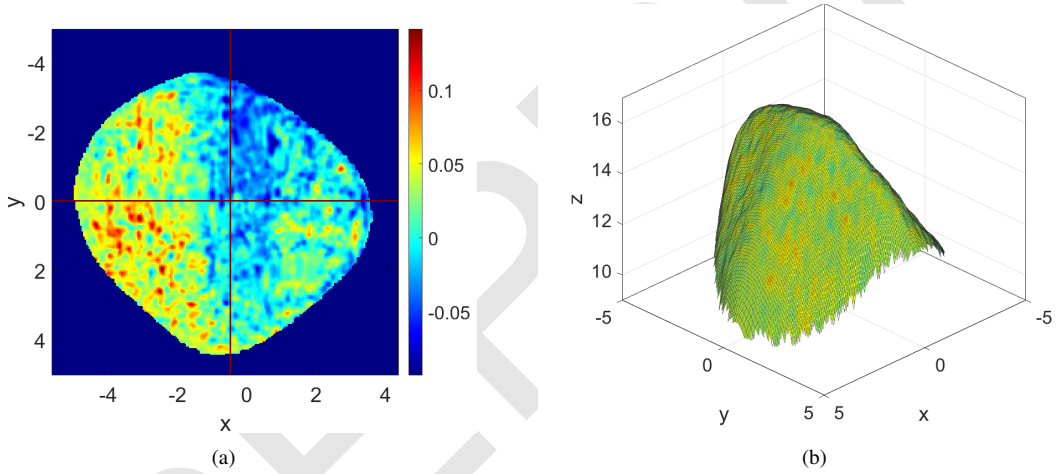


Figure 26: (a) Color map of the difference $v_z^{\mathsf{D3}'}$ and (b) 3D view. Values measured in mm.

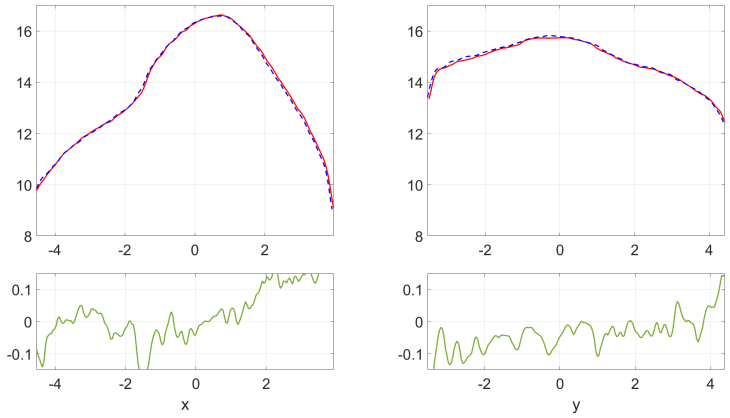


Figure 27: Top row shows slices of the teeth $\mathsf{D1_A}$ (solid red line) and $\mathsf{D1_B}$ (dashed blue line) whereas the bottom row shows $v_z^{\mathsf{D1}'}$. Left and right columns show the slices $y = -0.06$ and $x = -0.47$, respectively.

are 0.0130 mm and 0.0293 mm, respectively. It should be noted that in the ideal case, namely a comparison between a single scan and itself, all of these values should be theoretically equal to zero. Therefore, it can be stated that the nearer the parameters are to zero, the more precise the adjustment will be. It is also crucial to examine the maximum positive and negative error, given that, despite the low mean values, a considerable positive or negative error value would indicate a discrepancy in a specific region between the two models adapted to each tooth scan. For the entire tooth surface, the minimum and maximum values are $-0.111$ mm and 0.1416 mm, respectively, indicating that these values are sufficiently small to meet the precision requirements of the tooth comparison system.

The results demonstrate that the proposed method is sufficiently precise to facilitate comparisons between scans of teeth. This will enable the future utilization of this method to compare two distinct teeth, with the AIDDA® procedure detailed in Section 1, namely a master tooth carved by the dentistry instructor and a tooth carved by the dentistry student. Consequently, the discrepancy between both tooth carvings can be automatically and numerically evaluated in order to ascertain and quantify the errors made by the student and to assess their learning process and improvement.

Future lines of work include testing the method on additional pairs of teeth, in order to ascertain whether any modifications to the deformable model are required in accordance with the morphology of the tooth under analysis. On the other hand, given that the proposed approach entails the analysis of the upper part of the tooth, in the event of carving the sides of the teeth it would be necessary to apply two deformable models: the current model, which adapts to the upper surface, and another cylindrical deformable model to characterize the lateral sides of the teeth. Furthermore, it may be valuable to refine the model for areas with abrupt concavities, which may require a higher resolution of the model in these specific areas of the teeth.


## Funding

This work has been supported by the program "+Spin Off 21/22" of "Consejería de Empresa, Industria y Portavocía. Región de Murcia. Spain".


## Conflicts of Interest

The authors declare no conflict of interest.

## Author contributions

Conceptualization R.M.R., R.V.M., R.B.V.; Data curation R.M.R., R.B.V.; Formal analysis R.B.V., R.V.M.; Funding acquisition R.M.R.; Investigation R.B.V., R.V.M.; Methodology R.B.V., R.V.M.; Project administration R.M.R.; Resources R.M.R.; Software R.V.M., R.B.V.; Supervision, R.M.R., R.B.V., R.V.M.; Validation R.M.R., R.B.V., R.V.M.; Visualization R.B.V., R.V.M.; Roles/Writing - original draft R.V.M., R.B.V.; Writing - review & editing R.M.R., R.B.V., R.V.M.

## References


[1] M. Duan, S. Lv, B. Fan, W. Fan, Effect of 3D printed teeth and virtual simulation system on the pre-clinical access cavity preparation training of senior dental undergraduates, BMC Medical Education 24 (1) (2024) 913.

[2] Y. Fayyaz, M. Ali, R. Ullah, M. S. Shaikh, Applications of 3D-printed teeth in dental education: A narrative review, Journal of Taibah University Medical Sciences (2024).

[3] A. Mahrous, A. Elgreatly, F. Qian, G. B. Schneider, A comparison of pre-clinical instructional technologies: natural teeth, 3D models, 3D printing, and augmented reality, Journal of dental education 85 (11) (2021) 1795–1801.

[4] H.-J. Kong, Y.-L. Kim, Application of artificial intelligence in dental crown prosthesis: a scoping review, BMC Oral Health 24 (1) (2024) 937.

[5] C. Arnold, L. Riß, J. Hey, R. Schweyen, Dimensional accuracy of different three-dimensional printing models as a function of varying the printing parameters, Materials 17 (14) (2024) 3616.

[6] M. Czajkowska, E. Walejewska, Ł. Zadrożny, M. Wieczorek, W. Święszkowski, L. Wagner, E. Mijiritsky, J. Markowski, Comparison of dental stone models and their 3D printed acrylic replicas for the accuracy and mechanical properties, Materials 13 (18) (2020) 4066.

[7] K. Son, W.-S. Lee, K.-B. Lee, Effect of different software programs on the accuracy of dental scanner using three-dimensional analysis, International Journal of Environmental Research and Public Health 18 (16) (2021) 8449.

[8] K. Son, K.-b. Lee, Effect of tooth types on the accuracy of dental 3D scanners: An in vitro study, Materials 13 (7) (2020) 1744.
[9] E. G. Sultanoğlu, B. K. Eroğlu, Comparison of the accuracy and precision in digital scans for implant-supported maxillary hybrid prosthesis: In vitro study (2023).
[10] P. D. Badillo, V. A. Parfenov, Accuracy of alignment procedures used for the creation of 3D models, in: 2022 Conference of Russian Young Researchers in Electrical and Electronic Engineering (ElConRus), IEEE, 2022, pp. 1103–1106.
[11] A. Wen, N. Xiao, Y. Zhu, Z. Gao, Q. Qin, S. Shan, W. Li, Y. Sun, Y. Wang, Y. Zhao, Spatial trueness evaluation of 3D-printed dental model made of photopolymer resin: Use of special structurized dental model, Polymers 16 (8) (2024) 1083.
[12] D. Wu, J. Jiang, J. Wang, S. Zhou, K. Qian, Accuracy evaluation of dental CBCT and scanned model registration method based on pulp horn mapping surface: an in vitro proof-of-concept, BMC Oral Health 24 (1) (2024) 827.
[13] P. Sahu, S. Gerber, Q. Zhao, T. Nguyen, M. McCormick, B. Paniagua, J. Vicory, Thin shell demons for dental scan registration, in: Medical Imaging 2022: Image Processing, Vol. 12032, SPIE, 2022, pp. 751–758.
[14] M. Revilla-León, A. Gohil, A. B. Barmak, A. Zandinejad, A. J. Raigrodski, J. Alonso Pérez-Barquero, Best-fit algorithm influences on virtual casts' alignment discrepancies, Journal of Prosthodontics 32 (4) (2023) 331–339.
[15] X. Amezua-Lasuen, M. Iturrate-Mendieta, J. A. Oriozabala-Brit, X. Garikano-Osinaga, I. Martin-Amundarain, E. Solaberrieta-Mendez, Best-fit alignment in the digital dental workflow, in: Advances in Design Engineering: Proceedings of the XXIX International Congress INGEGRAF, 20-21 June 2019, Logroño, Spain, Springer, 2020, pp. 202–211.
[16] R. Li, H. Chen, Y. Wang, Y. Sun, Suitability of the triple-scan method with a dental laboratory scanner to assess the 3D adaptation of zirconia crowns, The Journal of Prosthetic Dentistry 125 (4) (2021) 651–656.
[17] N. Loumprinis, S. Michou, C. Rahiotis, Different methods of scan alignment in erosive tooth wear measurements: An in vitro study, Dentistry Journal 12 (2) (2024) 34.
[18] J. Liu, Y. Liu, J. Wang, X. Zuo, X. Wang, Y. Zhang, H. He, Dental measurements based on a three-dimensional digital technique: A comparative study on reliability and validity, Archives of Oral Biology 124 (2021) 105059.
[19] S. Akyalcin, D. J. Dyer, J. D. English, C. Sar, Comparison of 3-dimensional dental models from different sources: diagnostic accuracy and surface registration analysis, American Journal of Orthodontics and Dentofacial Orthopedics 144 (6) (2013) 831–837.
[20] M. Javaid, A. Haleem, L. Kumar, Current status and applications of 3D scanning in dentistry, Clinical Epidemiology and Global Health 7 (2) (2019) 228–233.
[21] F. Cuevas, M. R. Navarro, M. G. Salido, M. R. Villegas, Metrology and digital image processing in dentistry, in: Digital Image Processing-Latest Advances and Applications, IntechOpen, 2023.
[22] C.-W. Wang, C.-T. Huang, J.-H. Lee, C.-H. Li, S.-W. Chang, M.-J. Siao, T.-M. Lai, B. Ibragimov, T. Vrtovec, O. Ronneberger, et al., A benchmark for comparison of dental radiography analysis algorithms, Medical image analysis 31 (2016) 63–76.
[23] A. B. Nulty, 3D printing part 1-a history and literature review of 3D printing in dentistry (2021).
[24] J. M. Granero-Marín, R. Melendreras-Ruiz, R. Melendreras-Ruiz, D. Riera-Álvarez, R. Jiménez-Soto, n. García-Collado, Model for teaching in dental disciplines. Patent number WO2020208284, `https://patentscope.wipo.int/search/es/detail.jsf?docId=WO2020208284` (2020).
[25] F. Hunter, Dental models. Patent number WO1997034278, `https://patentscope.wipo.int/search/es/detail.jsf?docId=WO1997034278` (1997).
[26] F. U. S. Antonio, AIDDA Automated International Dental Dexterity Algorithm. Registered trademark M4150139, `https://branddb.wipo.int/en/similarname/brand/ES5020210M4150139` (1997).
[27] P. Soille, Morphological Image Analysis: Principles and Applications, 2nd Edition, Springer-Verlag, 2003.
[28] P. E. Gill, W. Murray, M. H. Wright, Numerical linear algebra and optimization, SIAM, 2021.
[29] M. Kass, A. Witkin, D. Terzopoulos, Snakes: Active contour models, Int. Journal of Computer Vision 1 (4) (1988) 321–331.
[30] D. Terzopoulos, Deformable models: classic, topology-adaptive and generalized formulations, in: S. Osher, N. Paragios (Eds.), Geometric Level Set Methods in Imaging, Vision and Graphics, Springer-Verlag New York, Inc., 2003, Ch. 2, pp. 21–40.
[31] A. S. El-Baz, R. Acharya, M. Mirmehdi, J. S. Suri (Eds.), Multi Modality State-Of-The-Art Medical Image Segmentation and Registration Methodologies, Volumen 1, Springer, 2011.
[32] J. Liang, T. McInerney, D. Terzopoulos, United snakes, Medical Image Analysis 10 (2) (2006) 215–233.
[33] I. N. Bankman (Ed.), Handbook of Medical Image Processing and Analysis, Elsevier, Academic Press, 2008.
[34] L. Weruaga, R. Verdú, J. Morales, Frequency domain formulation of active parametric deformable models, IEEE Trans. Pattern Analysis Machine Intelligence 26 (12) (2004) 1568–1578.
[35] R. Berenguer-Vidal, R. Verdú-Monedero, J. Morales-Sánchez, Design of B-spline multidimensional deformable models in the frequency domain, Mathematical and Computer Modelling 57 (7-8) (2013) 1942–1949.
[36] R. Berenguer-Vidal, R. Verdú-Monedero, R. M. Menchón-Lara, A. Legaz-Aparicio, Comparison of finite difference and B-spline deformable models in characterization of 3D data, in: Interplay Between Natural and Artificial Computation IWINAC: 5th Int. Conf., Vol. 7931 of Lecture Notes in Computer Science (LNCS), Springer Berlin / Heidelberg, 2013, pp. 230 – 240.
[37] R. Berenguer-Vidal, R. Verdú-Monedero, J. Morales-Sánchez, Convergence analysis of multidimensional parametric deformable models, Computer Vision and Image Understanding 135 (2015) 157–177.
[38] R. Verdú-Monedero, J. Morales-Sánchez, L. Weruaga, Convergence analysis of active contours, Image and Vision Computing 26 (8) (2008) 1118 – 1128.